Available online at www.sciencedirect.com
SCIENCE DIRECT®
Polymer 45 (2004) 1147–1157
polymer
www.elsevier.com/locate/polymer

# Fracture resistance of mineral reinforced polyamide 6

Christopher J.G. Plummer[a,*], Muriel Mauger[b], Philippe Béguelin[b], Gilles Orange[c], Joël Varlet[d]

[a]Ecole Polytechnique Fédérale de Lausanne (EPFL), Laboratoire de Technologie des Composites et Polymères (LTC), Institut des Matériaux, Lausanne CH-1015, Switzerland
[b]Ecole Polytechnique Fédérale de Lausanne (EPFL), Laboratoire des Polymères (LP), Institut des Matériaux, Lausanne CH-1015, Switzerland
[c]CRA, Rhodia-Recherches, 52 rue de la Haie Coq, 93308 Aubervilliers, France
[d]CRL, Rhodia-Recherches, 85 rue des Frères Perret, BP 62-69192 Saint-Fons Cedex, France

Received 29 July 2003; accepted 2 December 2003

**Abstract**

Tensile tests have been carried out over a wide range of test speeds on compact tension specimens of polyamide 6 containing spherical silica particles, whose size and content had been adjusted to give optimum impact performance in conventional impact tests after conditioning at 50% relative humidity. The tensile test results confirmed there to be a significant improvement in the high speed crack initiation resistance at room temperature and at high moisture contents on addition of the silica particles. However, at low moisture contents and/or temperatures well below the glass transition temperature, the crack initiation resistance was reduced. It is hence inferred that for the chosen silica particle distribution, toughening requires a certain minimum level of matrix ductility in order to be effective.


*Keywords:* Polyamide 6; Fracture; Mineral reinforcement

## 1. Introduction

Commercial thermoplastics often contain a mineral filler, whose function is typically to reduce their price and increase their dimensional stability, stiffness, heat deflection temperature and, in some cases, impact resistance. Optimization involves controlling the size distribution, geometry, dispersion and spatial separation of the filler particles and the properties of the interface between the particle and the polymer matrix. However, the relationship between these parameters and the impact resistance of mineral filled polymers remains unclear, and there are relatively few examples of polymers whose impact performance has been significantly improved by filler addition. Even in the case of rubber modified polymers, which have been extensively investigated over the last 20 years or so [1–3], current practice is as much based on empirically established criteria as it is on a detailed understanding of the underlying mechanisms. There is nevertheless a broad consensus according to which the role of the modifier particles is to activate deformation modes capable of dissipating energy in an extended damage zone around stress concentrations when the material is subject to mechanical loading. In thermoplastics, plasticity may take the form of homogeneous shear or crazing, depending on the matrix and the stress state. The formation of crazes is associated with globally brittle behaviour in unmodified polymers because it is highly localized and leads to limited energy dissipation [4]. It is therefore sometimes argued that the role of the modifier in brittle thermoplastics is to promote the formation of large numbers of crazes in the vicinity of a stress concentration, so that there is an increase in overall energy dissipation. However, even in systems where rubber modification leads to a significant increase in the craze density during tensile deformation, the accompanying increase in toughness may include a significant contribution from homogeneous shear deformation, favoured by local constraint release in the presence of cavities and crazes [5,6].

If localized deformation is activated by cavitation or debonding of the modifier, it is widely assumed that this should ideally occur when the local ligament stress is close to the effective $\sigma_y$. In rubber toughened polymers, the cavitation stress is controlled by adapting the particle size,

* Corresponding author. Tel.: +41-21-693-28-56; fax: +41-21-693-58-68.
*E-mail address:* christopher.plummer@epfl.ch (C.J.G. Plummer).

0032-3861/$ - see front matter © 2003 Elsevier Ltd. All rights reserved.
doi:10.1016/j.polymer.2003.12.022

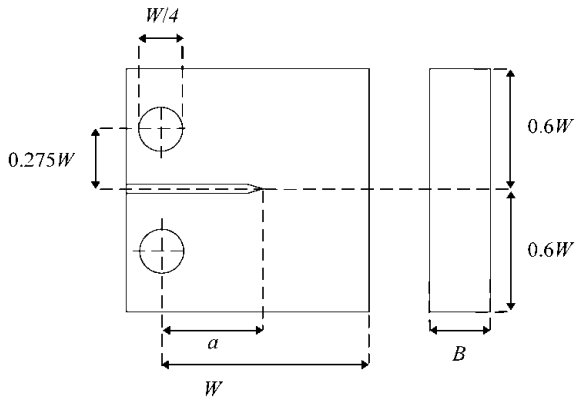


Fig. 1. The compact tension specimen geometry.

the particle–matrix adhesion and the particle elastic properties. The absolute interparticle distance also appears to play an important role in the efficient activation of dissipative deformation mechanisms in certain semicrystalline systems, including polyamide 6 (PA6) [7–11]. In general, one opts for good particle–matrix adhesion and a particle elastic modulus well below that of the matrix. The resulting local hydrostatic stress concentrations then lead to internal cavitation of the rubber during deformation [2]. However, rubber toughening is incompatible with maintaining high levels of overall rigidity, which provides part of the motivation for using mineral fillers. With mineral fillers, cavity formation may be induced and controlled by modifying the debonding threshold of the particle matrix interface. Given that the deformation of the modifier itself contributes little to the overall dissipation in rubber toughened polymers, one might therefore expect similar increases in toughness with an appropriate size distribution and dispersion of mineral particles. This has indeed been demonstrated under certain conditions, which suggests that simultaneous improvement in modulus and impact resistance can be designed for in these materials [12–14].

PA6, chosen for investigation here, is a semicrystalline polymer in which hydrogen bonding leads to a relatively high glass transition temperature, $T_g$ (about 47 °C), and melting point, $T_m$ (about 220 °C), and improved mechanical properties compared with those of commodity polyolefins. PA6 also interacts strongly with water and, under ambient conditions, contains sufficient humidity to induce a significant reduction in $T_g$ and enhanced ductility. Preliminary work has indicated significant improvements in the impact resistance of PA6 containing spherical silica particles when it is conditioned at 50% relative humidity (RH), depending on the particle size distribution and content [15]. However, no reinforcement has been observed in dry specimens. This has important technological implications, moulded parts' generally being dry immediately after fabrication, for example, and it raises questions regarding the low $T$ performance of silica modified PA6, which is also of practical concern. The aim of the present work has therefore been to extend these investigations of the influence of silica on the fracture resistance of PA6 through the systematic study of the effects of test speed, $v$, RH and $T$. To this end, fracture mechanics-based tensile testing has been carried out using hydraulic tensile test apparatus modified to permit quasi-static analysis over a very wide range of deformation rates, including the narrow range of effective $v$ characteristic of conventional impact tests [16,17]. As an aid to interpreting the results, the micromechanisms of crack tip deformation have also been investigated, with emphasis on determining the extent to which the global behaviour is associated with matrix–particle debonding. It is thus hoped to gain new insight into the extent to which the effective impact resistance over a wide range of conditions can be improved by mineral filler addition in PA6.

## 2. Experimental

### 2.1. Materials

The materials tested were:

1. unmodified PA6, with a weight average molar mass, $M_w$, of approximately 32,000 g mol$^{-1}$ and a polydispersity of approximately 2;
2. the same PA6 matrix containing approximately 10 wt% spherical silica particles ('Stöber' silica KEP50 provided by Nippon Shokubai) of 0.5 μm in diameter, introduced using a twin-screw extruder (PA6/S);
3. a commercial impact resistant PA6 containing approximately 20 wt% maleic anhydride grafted ethylene–propylene rubber (PA6/EPR).

Unless mentioned otherwise all the materials contained 0.1 wt% internal lubricant, and were provided by Rhodia in the form of injection moulded plaques. Compact tension (CT) specimens (24 × 24 × 4 mm$^3$) (Fig. 1) were machined from the plaques and a pre-crack was introduced to the notch tip using a fresh razor blade. The total pre-crack length was measured using a graduated magnifying glass before and after each test.

The machined specimens were conditioned at 30 and 50% RH in a controlled humidity oven (Heraeus). Conditioning was accelerated using the following parameters (adapted from ISO 1110): for 50% RH, 14 days at 70 °C/62% RH; for 30% RH, 14 days at 70 °C/30% RH. Conditioning at 0% RH refers to drying for a minimum of 16 h at 80 °C under vacuum. The specimens were weighed daily and conditioning was considered complete when less than 0.1% difference was found between results obtained on successive days. The mass uptake of the pure matrix was 1.6 and 3.6% for 30 and 50% RH, respectively. The corresponding mass uptake for the PA6/EPR (per unit matrix) was 1.6 and 3.5% but for the PA6/S it was 1.8 and 4.5%, a difference that may be accounted for by the hygroscopic nature of the filler itself (the silica particles

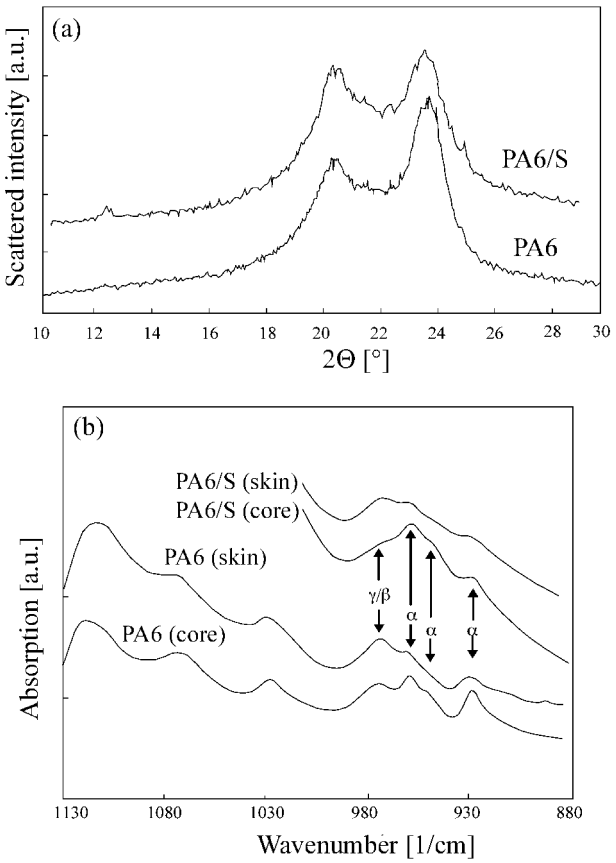


Fig. 2. (a) WAXS and (b) FTIR data for the materials indicated.

were –OH functionalized). Mechanical tests were performed within about an hour of removing the specimens from the oven.

### 2.2. Characterization

*Basic characterization*. Wide angle X-ray scattering (WAXS) was carried out using a Siemens Kristalloflex 805 diffractometer in reflection mode on cross-sections of the plaques (Cu Kα radiation, $\lambda = 1.54$ Å). Fourier transform infra-red spectroscopy (FTIR) was carried out using a Nicolet Magna-IR 560 spectrometer in attenuated total reflection (ATR) mode. Dynamic mechanical spectroscopy was carried out on $54 \times 12 \times 2$ mm$^3$ bars machined from the injection moulded plaques in three-point bending at $T$ between $-120$ and 200 °C, 1 Hz and a maximum strain of 0.2%, using a Rheometrics RSA II solids analyser.

*Mechanical testing*. Mode I fracture tests were carried out on the CT specimens using a Schenck servo-hydraulic test apparatus (Hydropuls POZ 1152), equipped with an environmental chamber. Specimen displacements at the loading points were in some cases measured directly using an optical extensometer, but since this system was not adapted for use with the environmental chamber, the displacements referred to in what follows were estimated from the position of the crosshead. At $v > 0.1$ m s$^{-1}$, an elastomeric pad was used to damp dynamic effects [16,17], and hence maintain quasi-static conditions up to the highest $v$ investigated (nominal values of 10 m s$^{-1}$). Under such conditions, a mode I stress intensity factor, $K_I$, may be calculated from

$$K_I = f[a/W]\frac{F}{B\sqrt{W}} \tag{1}$$

where $F$ is the force, $B$, the specimen thickness, $W$ is the specimen width (see Fig. 1) and

$$f[a/W] = \frac{2 + a/W}{1 - (a/W)^{3/2}}[0.886 + 4.64(a/W) - 13.32(a/W)^2 + 14.72(a/W)^3 - 5.6(a/W)^4]$$

where $a$ is the crack length [18–20]. Substitution of $F_{max}$ for $F$ in Eq. (1) then gives $K_{max}$. If the specimen response is linear elastic up to the maximum force, $K_{max} = K_{Ic}$, the plane strain mode I critical stress intensity factor for crack initiation, According to the standard test protocol [19], this criterion is satisfied if

$$B, a, W - a \geq 2.5\left(\frac{K_{max}}{\sigma_y}\right)^2 \tag{2}$$

where $\sigma_y$ is the yield stress. If Eq. (2) is not satisfied, $K_{max}$ cannot be considered to be a linear elastic fracture mechanics (LEFM) parameter. However, given that all the tests were carried out using the same specimen geometry and under comparable conditions, it remains a useful, albeit conservative measure of the evolution of the crack initiation resistance as a function of $v$ and $T$.

In Eq. (3), the data are plotted as a function of the loading rate

$$dK/dt = dF/dt\frac{f[a/W]}{B\sqrt{W}} \tag{3}$$

where $dF/dt$ is taken from the linear part of the stress strain curves. $dK/dt$ incorporates the geometric factor $f[a/W]$ and hence small variations in specimen geometry from one specimen to another. However, an approximate indication of the corresponding $v$ is also provided, and for convenience, reference will generally be made to $v$ rather than $dK/dt$ in Eq. (3). To provide an indication of the crack propagation behaviour of the specimens, ductile–brittle transitions are also referred to. The ductile–brittle transition is defined here as the transition from stable, or partly stable crack propagation (that is, $F > 0$ at displacements beyond that corresponding to $F_{max}$), to fully unstable crack propagation.

*Morphological characterization*. *Post mortem* fracture surfaces were gold coated and observed by scanning electron microscopy (SEM, Philips XLF-30 FEG-SEM) at 1 (secondary electron (SE) detector) and 5 kV (back-scattered electron (BSE) detector), with a working distance of between 6 and 10 mm. In CT specimens in which the

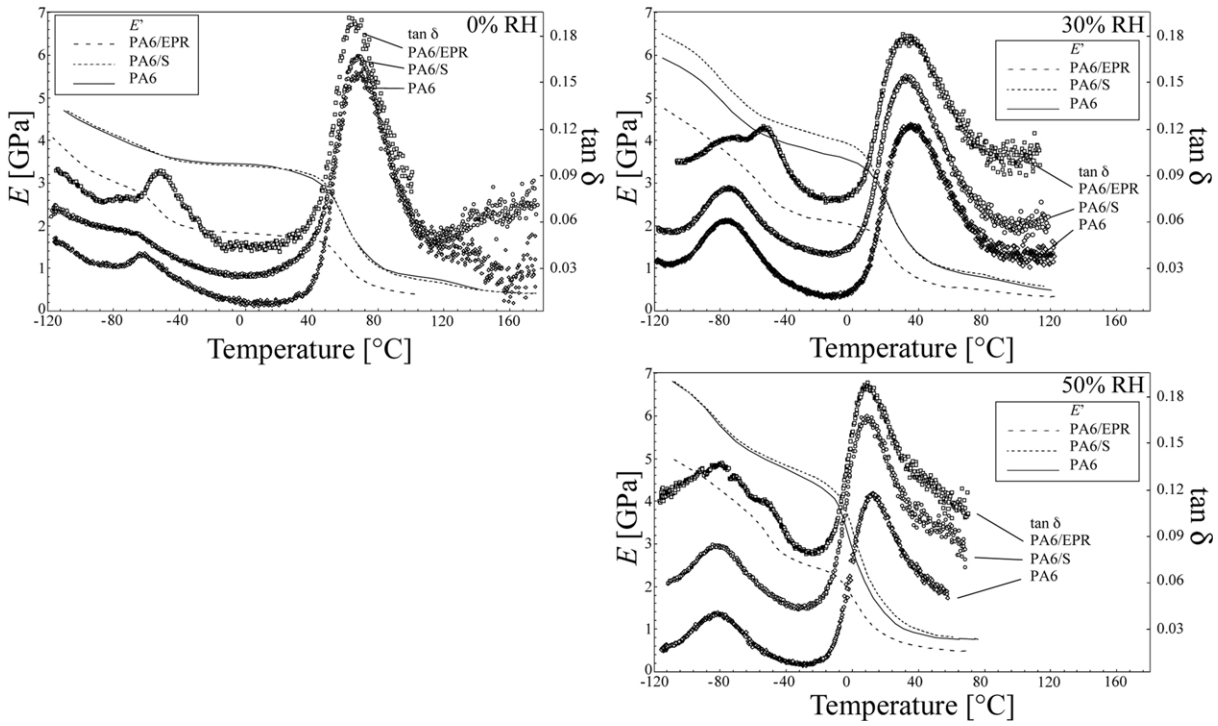


Fig. 3. Data for $E'$ and tan $\delta$ from three-point bend specimens conditioned at different RH and tested at 1 Hz (tan $\delta$ curves offset for clarity).

crack was arrested prior to total failure, surfaces exposed perpendicular to the crack plane by ultramicrotomy with a diamond knife (Reichert-Jung Ultracut E/Diatome 35° diamond knife) were also observed by SEM. This has the advantage of revealing the whole gradient of deformation up to the final fracture event. To minimize relaxation, the crack faces were wedged open under load with a block of PMMA prior to sectioning. To obtain partially cracked specimens from high $v$ tests, two specimens were tested in series, so that failure of one of the specimens instantaneously unloaded the other [17].

## 3. Results

Fig. 2(a) shows WAXS spectra for PA6 and PA6/S. The main features of the spectra for both materials were the two strong, well-separated reflections at $2\theta \approx 20$ and 24°, characteristic of the monoclinic α modification [21,22], and the absence of a strong peak at $2\theta \approx 22°$, characteristic of the γ and the β modifications [22]. The FTIR spectra, shown in Fig. 2(b), along with the positions of the absorption peaks corresponding to the α, β and γ modifications [23–25], confirmed the α phase to dominate in the cores of specimens of both PA6 and PA6/S. The peak at 975 $cm^{-1}$, which may be assigned to either the γ or the β modification, was also prominent in spectra taken from the specimen surfaces (skin), but an absorption peak at about 1000 $cm^{-1}$, generally associated with the γ modification, was absent [23–25].

Table 1
$T_\alpha$ (°C) for the different materials conditioned at different RH

| | Relative humidity | | |
|---|---|---|---|
| | 0% | 30% | 50% |
| PA6 | 68 | 34 | 14 |
| PA6/S | 67 | 31 | 10 |
| PA6/EPR | 67 | 32 | 12 |

Fig. 3 shows the variation of the storage modulus $E'$ and tan $\delta$ with $T$ at 1 Hz for PA6, PA6/S and PA6/EPR conditioned at three different RH. The main α relaxation peak ($T_\alpha \approx 70$ °C at 0% RH) and the secondary β relaxation peak ($T_\beta \approx -60$ °C at 0% RH) of the PA6 matrix are clearly identifiable, along with the α relaxation peak of the EPR at about −50 °C. $T_\alpha$ decreased with RH regardless of the presence of modifier particles, and there was a significant increase in the strength of the matrix β relaxation with increasing RH in all the materials, believed to be associated with non-H-bonded polar groups and/or $-OH/NH_2$ interactions [26,27]. $T_\beta$ was nevertheless relatively insensitive to RH, its decreasing by about 20 K as RH increased from 0 to 50%, whereas $T_\alpha$ decreased by about 55 K (Table 1). At 0% RH, the β relaxation was also broader and less intense in PA6/S than in PA6, but the behaviour of the two materials became very similar at 30 and 50% RH.

### 3.1. Fracture behaviour

Fig. 4(a) shows fracture data for several lots of the different materials, independently moulded and conditioned

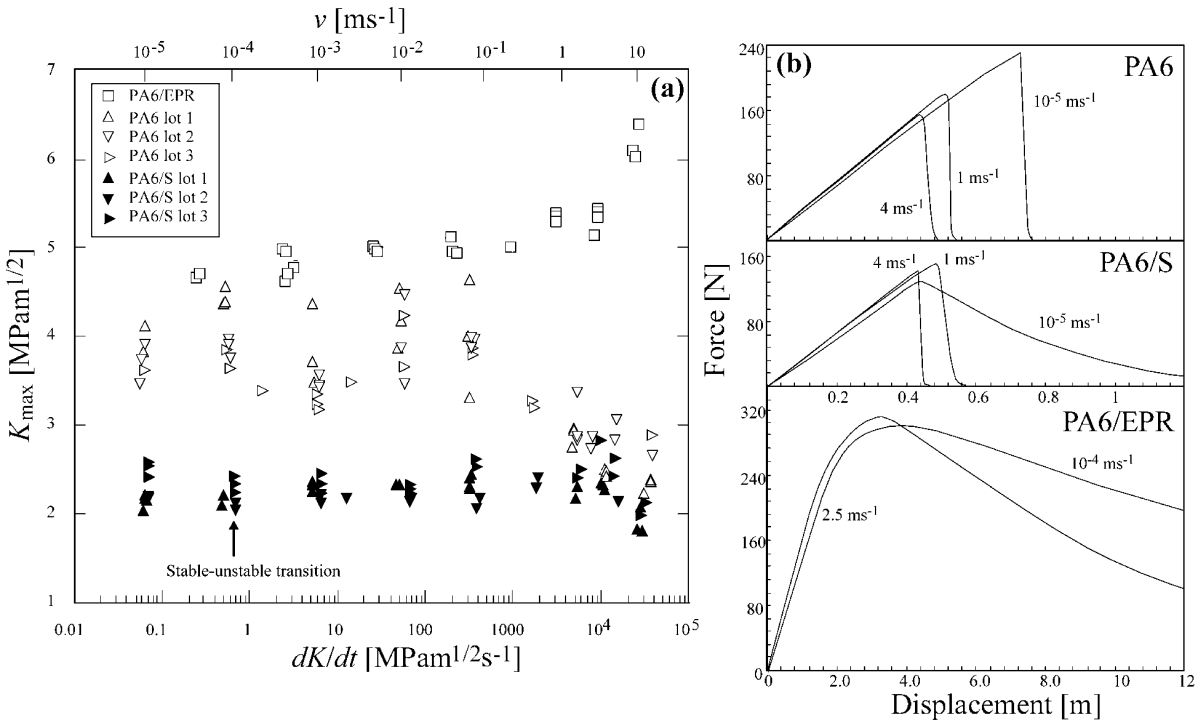


Fig. 4. $K_{max}$ for the different materials conditioned at 0% RH.

at 0% RH (in the case of PA6/S, the particle concentrations were slightly different: lot 1: 9.5 wt% (no lubricant), lot 2: 10.6 wt%, lot 3: 12 wt%). PA6 underwent unstable fracture over the whole range of $v$ investigated, but in PA6/S, stable crack propagation beyond the force maximum was observed at $v \leq 10^{-4}$ m s$^{-1}$ (Fig. 4(b)), and a ductile–brittle transition could therefore be defined in this case. Nevertheless, according to the test protocol cited in Section 2, $K_{max} = K_{Ic}$ for both PA6 and PA6/S at all $v$, and, although $K_{max}$ was consistently higher in PA6 than in PA6/S, it tended to a value of about 2 MPa m$^{1/2}$ in both materials for $v > 1$ m s$^{-1}$. In PA/EPR, on the other hand, for which ductile behaviour was observed throughout (Fig. 4(b)), and valid $K_{Ic}$ data could not be determined using the present geometry, $K_{max}$ increased monotonically with $v$. This was attributed to an increase in $\sigma_y$ with deformation rate.

*Influence of RH*. The absolute values of $K_{max}$ for PA6 were not strongly dependent on RH, as shown in Fig. 5(a), although there was substantial experimental scatter. In specimens conditioned at 30 and 50% RH, $K_{max}$ again tended to a value of about 2 MPa m$^{1/2}$ at high $v$. However, in contrast with the behaviour of specimens conditioned at 0% RH, a clear ductile–brittle transition was observed at $v$ between 0.01 and 0.03 m s$^{-1}$, and between 0.01 and 0.1 m s$^{-1}$ in PA6 conditioned at 30 and 50% RH, respectively. There was hence a clear systematic trend towards ductile fracture as RH increased, consistent with humidity-induced plastification. At $v$ (or d$K$/d$t$) below the ductile–brittle transition, it was no longer possible to obtain valid $K_{Ic}$. Fig. 5(b) shows data for different lots of PA6/S conditioned at different RH. At 30% RH, a ductile–brittle transition was observed at $v$ between 0.1 and 0.2 m s$^{-1}$ in PA6/S, that is, at higher $v$ than in PA6. Moreover, the $K_{max}$ values obtained at low to intermediate $v$ substantially exceeded those in PA6. At 50% RH, the $K_{max}$ values obtained in PA6/S at low $v$ were closer to those in PA6, but the ductile–brittle transition was again shifted to higher $v$ (between 2.5 and 3.5 m s$^{-1}$). Fig. 5(c) shows the behaviour of PA/EPR at different RH. Although PA/EPR remained ductile throughout, $K_{max}$ decreased markedly with RH, and became significantly lower than in PA6 at low $v$, an effect that was attributed to a decrease in $\sigma_y$ in the presence of the EPR. However, the observed increase in $K_{max}$ with $v$ persisted over the whole range of RH so that the crack initiation resistance at high $v$ was comparatively good.

*Influence of T*. The changes in $T_\alpha$ with RH shown in Fig. 3 are expected to have a strong influence on $K_{max}$ as a function of absolute temperature near the transition. Conversely, the materials response at fixed $T - T_\alpha$ is expected to be less strongly dependent on RH. Fig. 6 shows $K_{max}$ for PA6, PA6/S and PA6/EPR conditioned at different RH and tested at $T - T_\alpha \approx 10$ K. The data for the different RH did indeed superpose, although there were significant departures at the highest $v$ for PA6/S, in that the specimens conditioned at 50% RH and tested at 25 °C showed a somewhat higher ductile–brittle transition speed than those conditioned at lower RH and tested at higher $T$.

The different materials were also tested at $T - T_\alpha \approx -45$ K, that is, at 25 °C for specimens conditioned at 0% RH ($T_\alpha \approx 70$ °C). The results are shown in Fig. 7. $K_{max} = K_{Ic}$ throughout for PA6 and PA6/S, and the $K_{max}$ values for PA6/S were consistently less than or equal

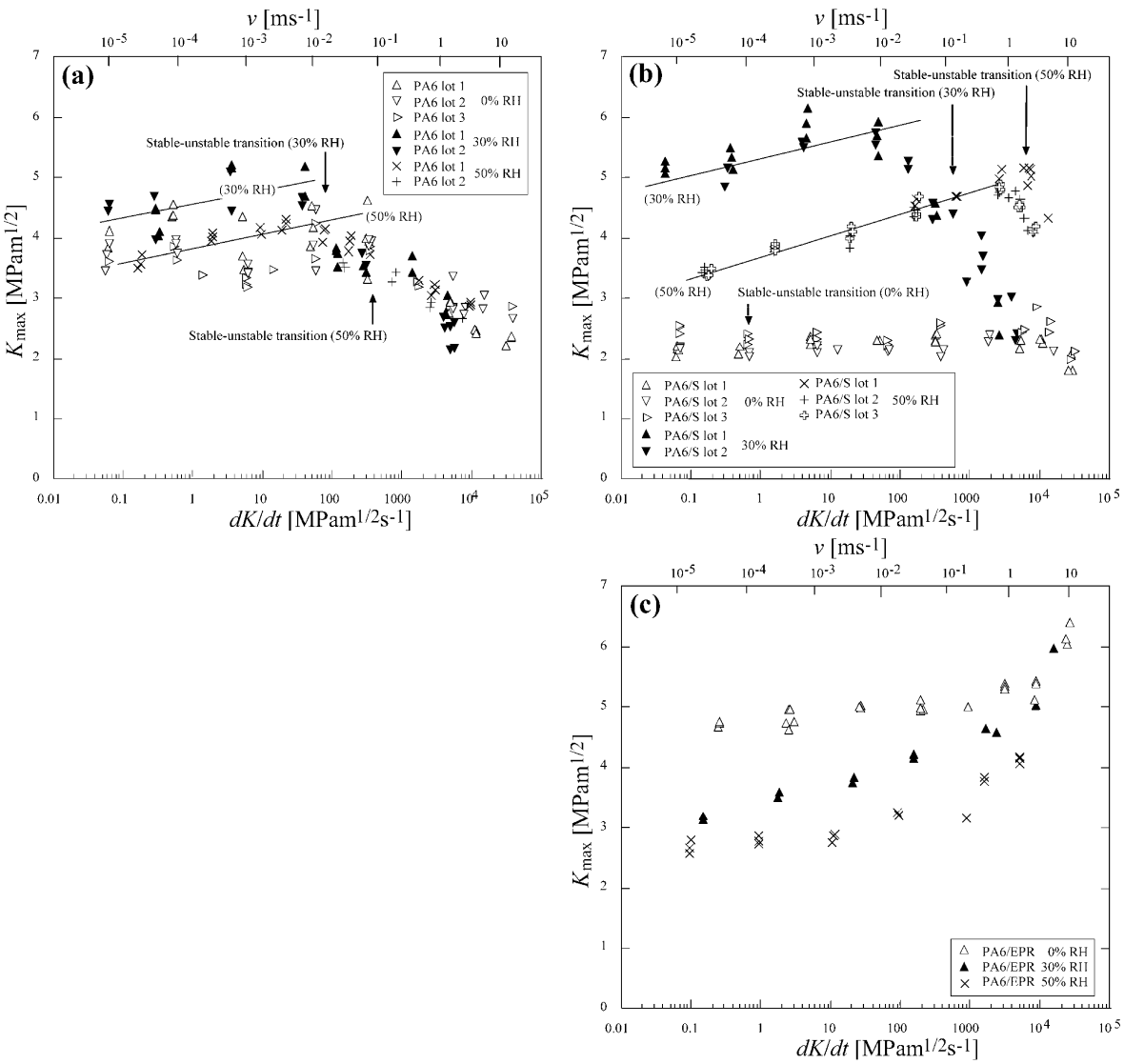


Fig. 5. $K_{max}$ for the different materials conditioned at different RH; (a) PA6, (b) PA6/S, (c) PA6/EPR. The loci of $K_{max}$ values for PA6 and PA6/S at 30 and 50% RH that did not satisfy the criterion for $K_{Ic}$ are given by the straight lines; at 0% RH all the data points for PA6 and PA6/S represent $K_{Ic}$ whereas PA6/EPR was ductile throughout.

to those for PA6, which suggested little or no toughening at any RH under these conditions, in spite of the transition to stable crack growth in PA6/S at low $v$ for 0% RH, referred to previously. Although $K_{max}$ in PA6/S varied little with RH, the data for PA6 did not superpose, and there were particularly marked changes in the behaviour of PA6/EPR, which showed a clear ductile–brittle transition at 30% RH, and became brittle at 50% RH over the whole range of $v$ investigated. The poor superposition in PA6 is assumed to reflect the influence of $T_\beta$ at $T \ll T_\alpha$. In the case of PA6/EPR, the proximity of the lowest test temperatures to $T_\alpha$ of the EPR domains (about $-50$ °C), is also expected to reduce the effectiveness of these latter as rubber modifiers.

*Microdeformation mechanisms*. Fig. 8(a) and (b) shows SEM images from the crack tip damage zone in PA6/S conditioned at 0 and 30% RH, respectively, and deformed at 25 °C and $v$ below the ductile–brittle transition speed. In the specimen conditioned at 0% RH and deformed at $10^{-5}$ m s$^{-1}$ (Fig. 8(a)), i.e. just below the transition, there was little blunting of the crack tip. Damage was in this case confined to a wedge-shaped zone, made up of nearly parallel rows of debonded particles, as shown in more detail in Fig. 9. On the other hand, in the specimen conditioned at 30% RH and deformed at 0.05 m s$^{-1}$ (Fig. 8(b)), which showed more ductile behaviour, particle–matrix debonding and extensive plastic deformation were visible in a roughly cylindrical zone centred on the crack tip. Such features were common to all regimes of fully ductile fracture in PA6/S, as illustrated further by the example in Fig. 10, which shows crack tip deformation in a specimen conditioned at 50% RH and deformed at 25 °C and $v \approx 10^{-4}$ m s$^{-1}$. Similarly, in the immediate vicinity of the ductile–brittle transition, damage was generally confined to a wedge-shaped zone of debonded particles, as shown in Fig. 11 for a specimen

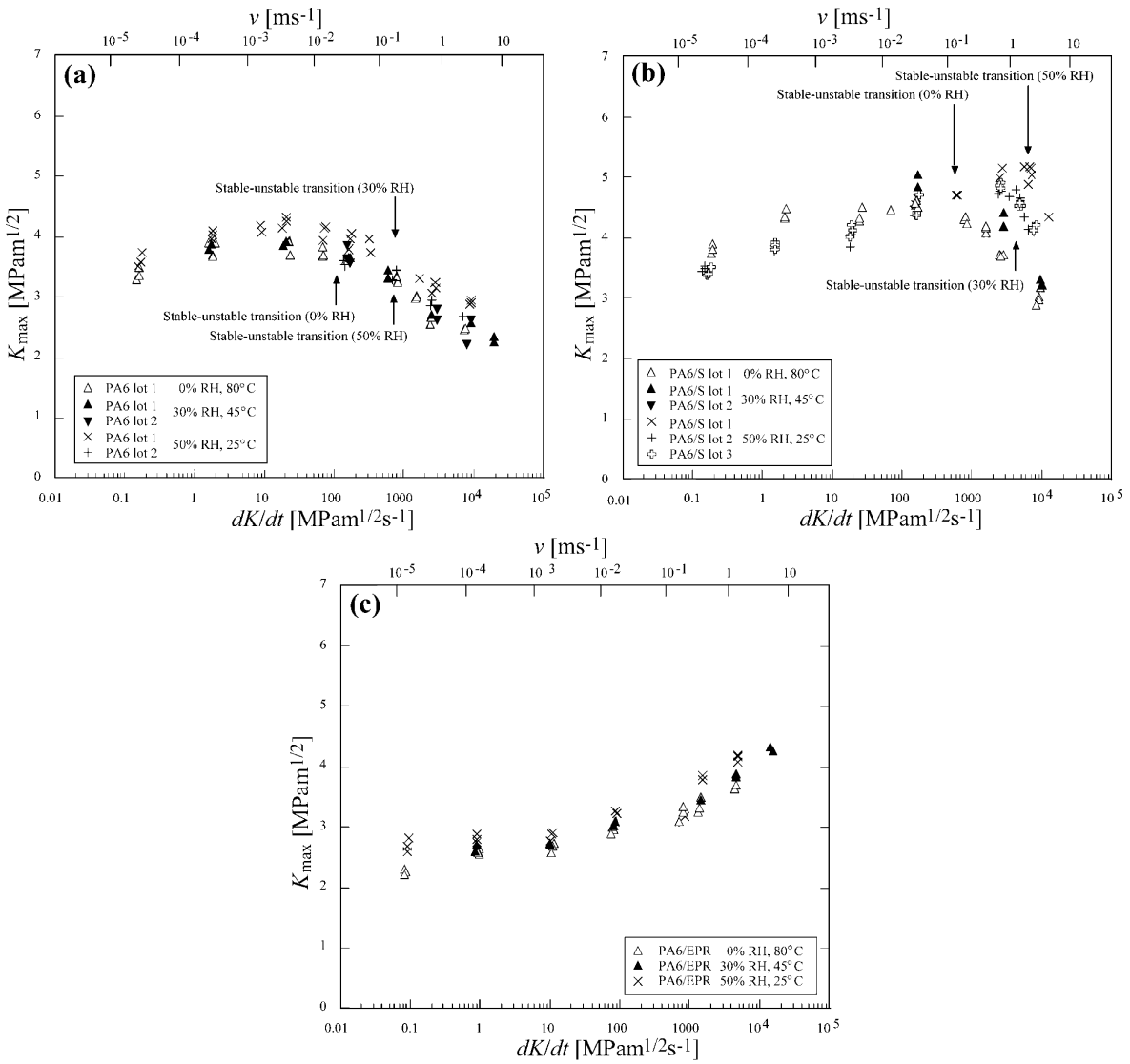


Fig. 6. $K_{max}$ for the different materials at $T_\alpha - T \approx 10$ K; (a) PA6, (b) PA6/S, (c) PA6/EPR.

conditioned at 50% RH and deformed at 25 °C and $v \approx 3$ m s$^{-1}$.

Fig. 12(a) shows the fracture surface of PA6/S conditioned at 0% RH and deformed at 25 °C and $10^{-3}$ m s$^{-1}$, in which plasticity was limited to a narrow region immediately adjacent to the tip of the pre-crack. In this region, aggregates of several particles were visible within dimples on the fracture surface. As $v$ decreased towards the ductile–brittle transition speed, two distinct zones of plasticity were often present: plastic dilation of cavities associated with single particles dominated the region of the fracture surface immediately adjacent to the tip of the pre-crack, whereas particle aggregates were more in evidence further from the crack tip. In specimens that showed fully ductile fracture, plastic dilation of cavities associated with single particles was present over the whole fracture surface, as shown in Fig. 12(b) for a specimen conditioned at 50% RH, and deformed at 25 °C and $10^{-4}$ m s$^{-1}$. The same trends were seen at other RH and $T$.

Fig. 13 shows, for comparison, images at different magnifications of microdeformation at the crack tip in a specimen of PA6/EPR that had undergone stable crack propagation (0% RH, 25 °C and $10^{-3}$ m s$^{-1}$). Although the EPR domains were not directly visible under the observation conditions employed in Fig. 13, there was clearly significant plastic deformation in the matrix, accompanied by extensive cavitation, which was assumed to be associated with the EPR.

## 4. Discussion

The overall picture that emerges from the results presented here is that modification of PA6 with silica particles can lead to significant impact toughening at high

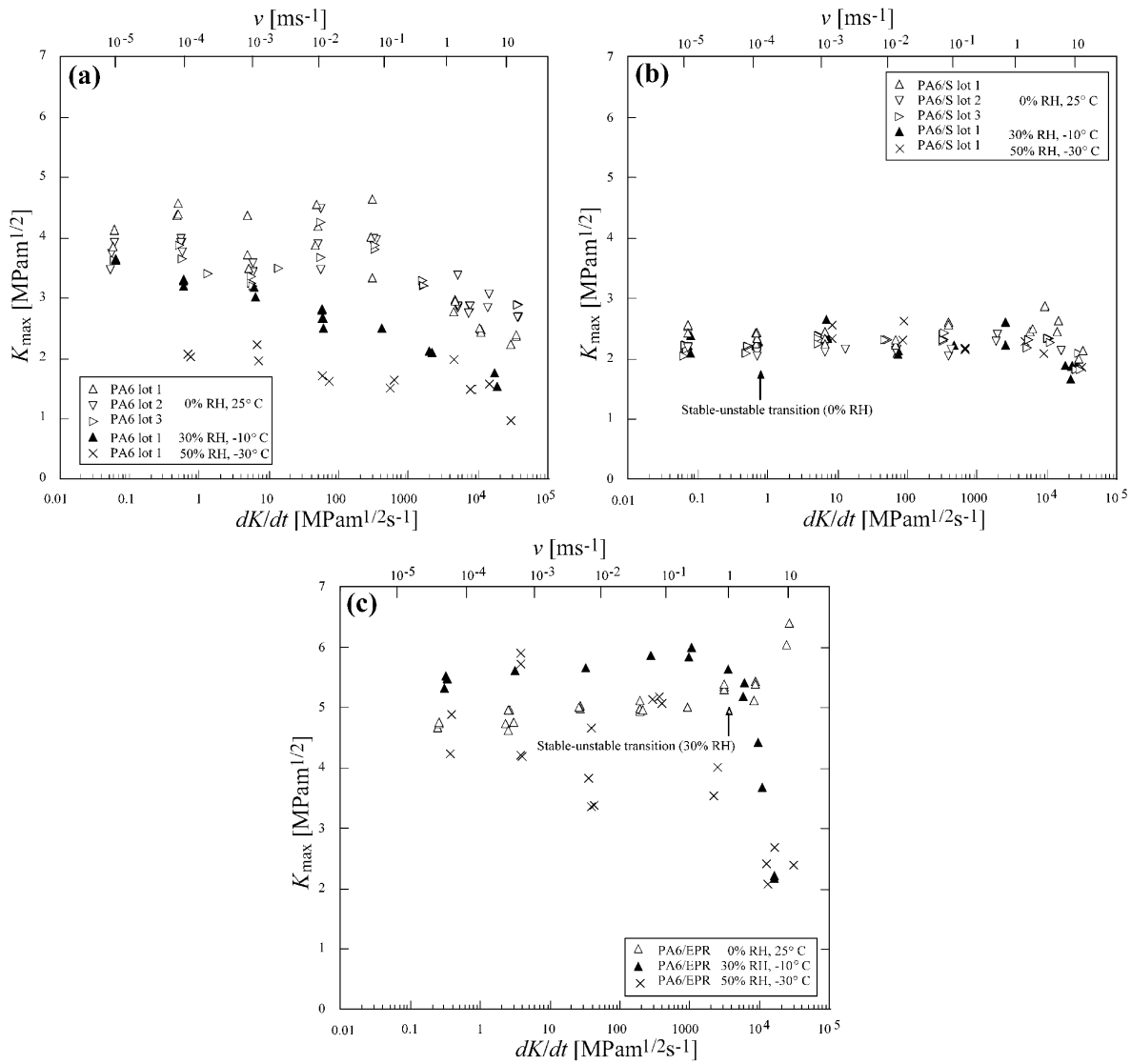


Fig. 7. $K_{max}$ for the different materials at $T_\alpha - T \approx -45$ K; (a) PA6, (b) PA6/S, (c) PA6/EPR.

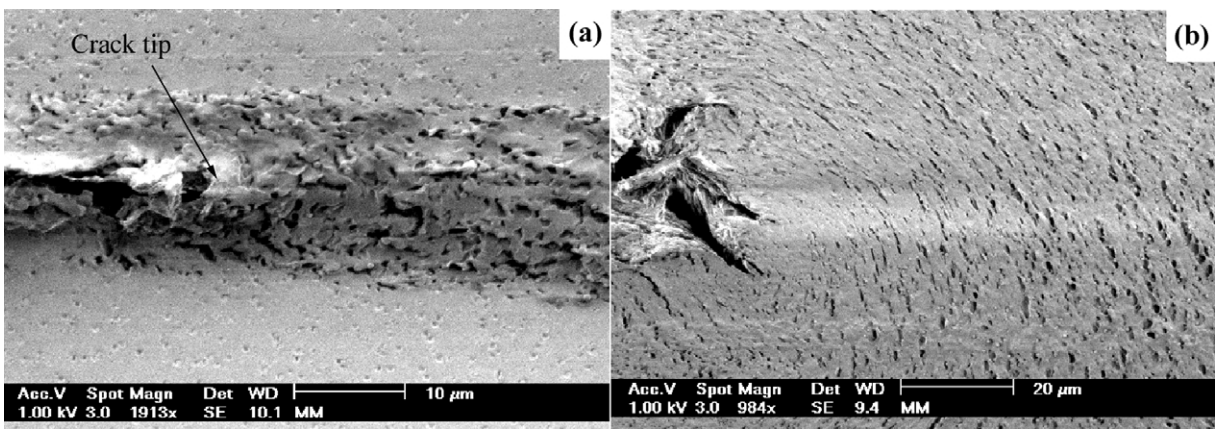


Fig. 8. Secondary electron images of sections through the crack tip damage zone: (a) PA6/S, 0% RH, 25 °C, $v = 10^{-5}$ m s$^{-1}$; (b) PA6/S, 30% RH, 25 °C, $v = 0.05$ m s$^{-1}$.

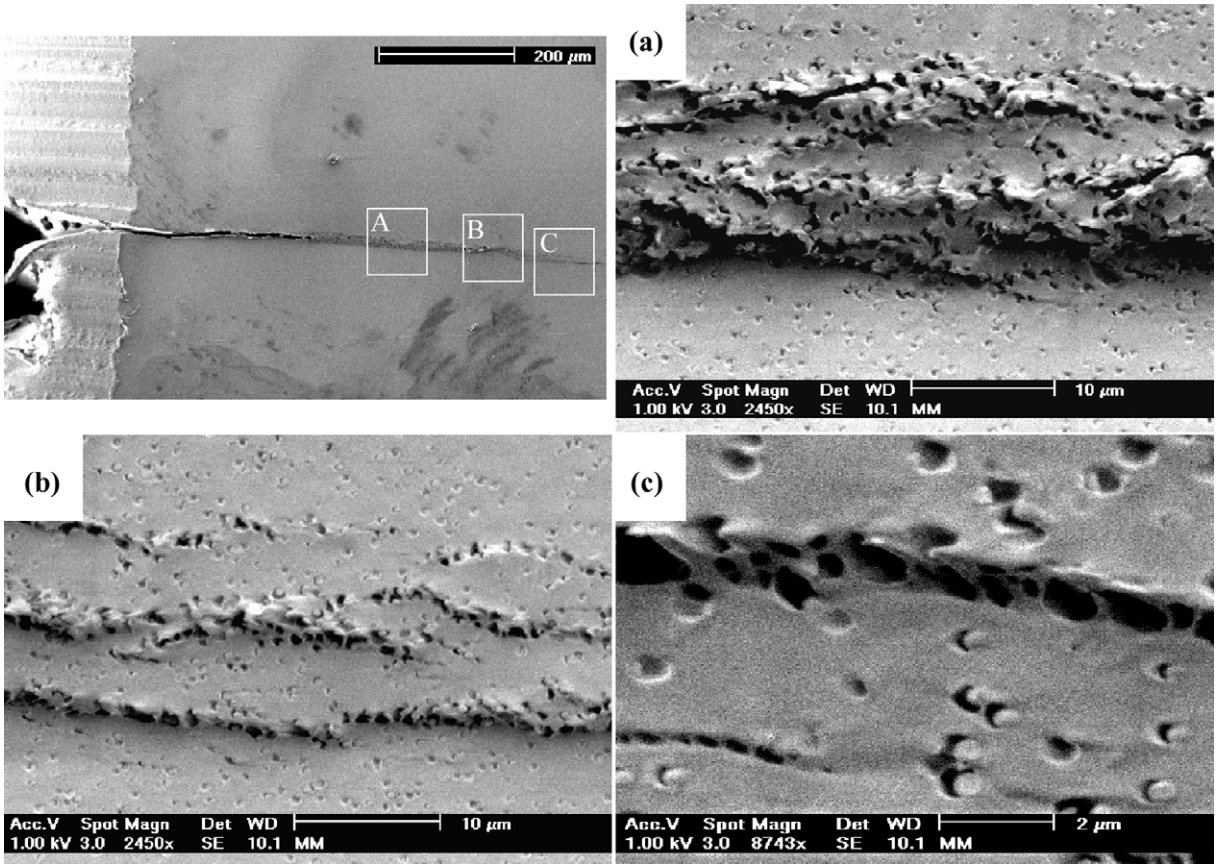


Fig. 9. Secondary electron images of a section through the crack tip damage zone in PA6/S, 0% RH, 25 °C, $v = 10^{-5}$ m s$^{-1}$, showing various details as indicated.

RH without the loss in stiffness associated with rubber modification. Moreover, the silica particles did not have an adverse effect on the low and intermediate speed fracture resistance at high RH, which was characterized by relatively ductile behaviour and stable crack propagation in both PA6 and PA6/S. In these regimes of ductile behaviour, $K_{max}$, increased roughly linearly with d$K$/d$t$ in and decreased with increasing RH (Fig. 5(a) and (b)). These trends were even more apparent in PA6/EPR, in which the regime of ductile behaviour was greatly expanded with respect to those in the other materials (Fig. 5(c)), although the stiffness, yield stress and absolute values of $K_{max}$ were relatively low.

The increased ductile–brittle transition speeds in PA6/S at high RH with respect to those in PA6 were accompanied by an extension of the regime in which $K_{max}$ increased linearly with d$K$/d$t$ to higher d$K$/d$t$. The observation that plastic deformation was correlated with particle debonding close to the ductile–brittle transition speed suggested this to be at least partly due to local plastic constraint release. It follows that the observed improvements were associated with conditions under which the matrix maintained a

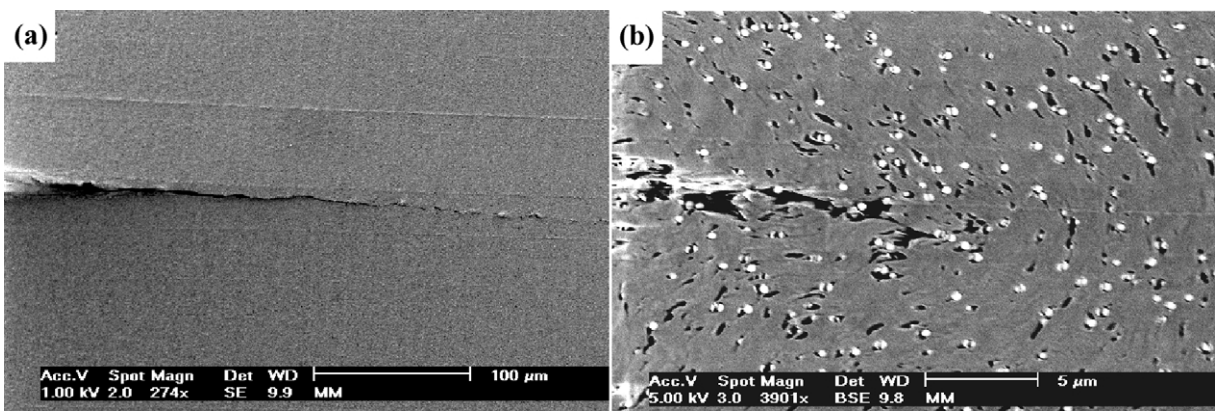


Fig. 10. Secondary and backscattered electron images of a section through the crack tip damage zone in PA6/S, 50% RH, 25 °C, $v = 10^{-4}$ m s$^{-1}$.

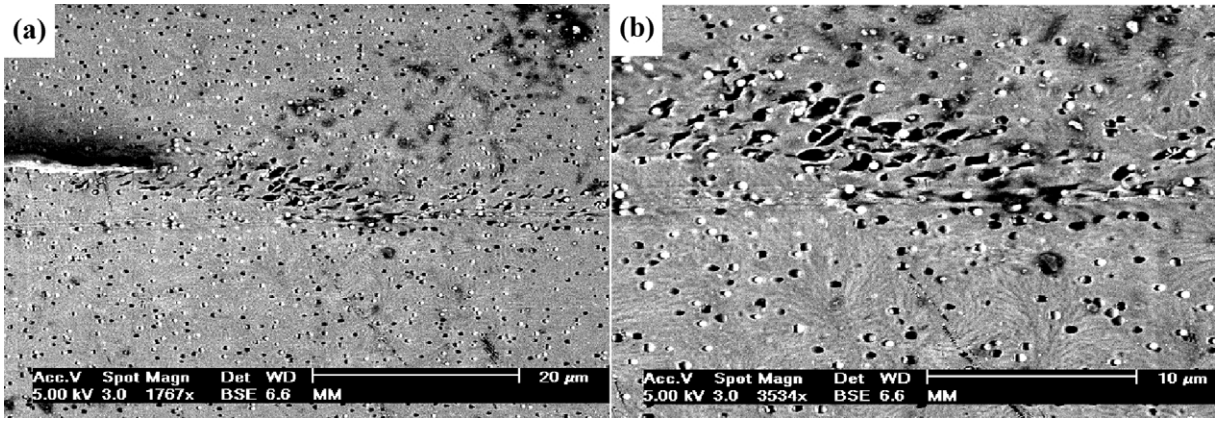


Fig. 11. Backscattered electron images from a section through the crack tip damage zone in PA6/S, 50% RH, 25 °C, $v \approx 3\ \mathrm{m\ s^{-1}}$.

relatively high degree of ductility. There was no evidence for modifications in the crystalline structure (Fig. 2) or correlations between the local lamellar orientation and the particle matrix interfaces, which have been invoked to account for the dependence of toughening on the ligament thickness in a variety of modified semicrystalline polymers, including PA6 [9–11]. Spherulite sizes were about an order of magnitude greater than the particle separations and the lamellar trajectories were oriented at arbitrary angles to the particle surfaces. It is perhaps significant that increased RH at $T_\alpha - T = 10\ \mathrm{K}$ led to substantial increases in the ductile–brittle transition speeds in PA6/S, although those in PA6 varied little (Figs. 6 and 14). This effect was attributed to a weakening of the PA6–silica interfaces at high RH owing to blocking of sites for hydrogen bonding by water molecules, and hence a reduced debonding threshold. It implies that optimized matrix–particle interfacial strength at high RH may not necessarily result in optimum performance at low RH, so that it would be of interest to investigate further the effect of systematic variations in interfacial strength in different regimes of RH and temperature using the present technique.

In the present case, not only was there no high speed toughening in PA6/S conditioned at 0% RH, for which the matrix was relatively brittle, but $K_{max}$ was also substantially reduced with respect to that of the matrix over most of the range of speeds investigated. The observation of particle clusters on the fracture surfaces indicated that this was because the particles acted collectively as defects in regimes of low matrix ductility. The overall behaviour was therefore consistent with the earlier impact results referred to in Section 1 [15], i.e. improvements in toughness in specimens conditioned at 50% RH but not at 0% RH. At 50% RH the effective test speed corresponding to impact tests was just above the ductile–brittle transition speed in PA6, and the toughening effect of PA/S was sufficient to push the ductile–brittle transition into the regime of impact speeds (i.e. an improvement of one to two orders of magnitude in the ductile–brittle transition speed).

## 5. Conclusions

The high speed test results presented here showed addition of spherical silica particles to a PA6 matrix to improve resistance to crack initiation at high RH, and shift the ductile–brittle transition to higher speeds. They were therefore consistent with earlier results from impact testing, which was used to determine the optimum size and separation of the particles for improved impact performance

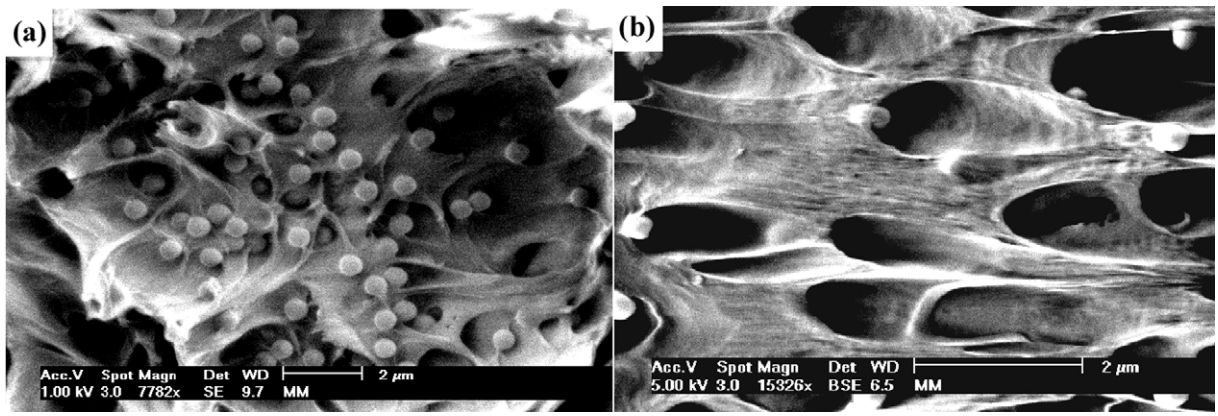


Fig. 12. Details from fracture surfaces: (a) PA6/S, 0% RH, 25 °C, $v = 10^{-3}\ \mathrm{m\ s^{-1}}$; (b) PA6/S, 50% RH, 25 °C, $v = 10^{-4}\ \mathrm{m\ s^{-1}}$.

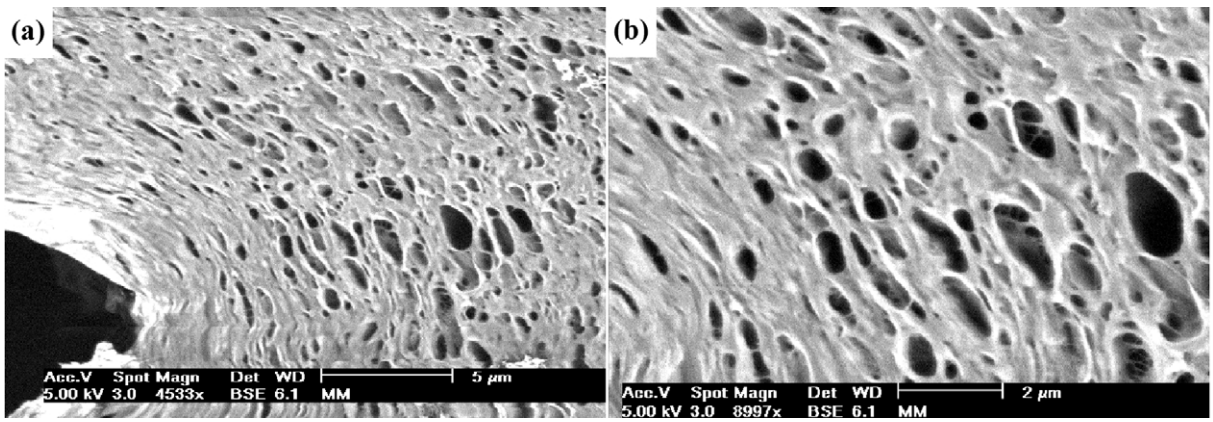


Fig. 13. Backscattered electron images from a section through the crack tip damage zone in PA6/EPR, 0% RH, 25 °C, $v = 10^{-3}$ m s$^{-1}$.

at high RH. They also confirmed a lack of significant toughening in dry specimens for the same particle distribution, and indeed the particles appeared to act as defects under these conditions. Results obtained at different $T$ showed similar trends, particularly above $T_\alpha$, where there was an approximate RH–$T$ equivalence for a reference temperature $T = T_\alpha$. Although this equivalence did not extend to $T \ll T_\alpha$, owing to the influence of the sub-$T_g$ β transition, the trend towards more brittle behaviour with decreasing temperature or RH persisted. This implies a certain amount of matrix ductility to be necessary if the present dispersions of silica particles are to be effective tougheners for PA6. The outlook for particle toughening in PA6 is nevertheless globally encouraging bearing in mind that the improvements at high RH were obtained without sacrificing stiffness or low speed crack resistance, and that there is scope for further optimization of the particle content and size distribution.

## Acknowledgements

The authors wish to thank J.-P. Marchand and R. Michel of Rhodia, and the Electron Microscopy Centre (CIME) of the EPFL, for their administrative and technical support respectively.

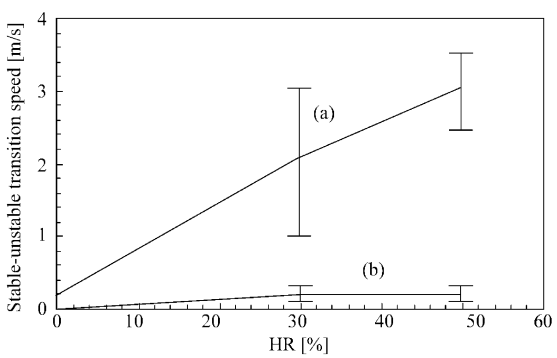


Fig. 14. Stable–unstable (ductile–brittle) transition speeds at $T_\alpha - T \approx 10$ K; (i) PA6, (ii) PA6/S.

## References

[1] Riew CK, Kinloch AJ, editors. Toughened plastics II, Washington, DC: ACS; 1996.
[2] Bucknall CB. Toughened plastics. London: Appl. Sci. Pub; 1977.
[3] Pearson RA, Sue H-J, Yee AF, editors. Toughening of plastics: advances in modelling and experiments. ACS Symposium Series 759, Washington, DC: ACS; 2000.
[4] Kramer EJ. Adv Polym Sci 1983;52–53:1.
[5] Magalhães AML, Borggreve RJM. Macromolecules 1995;28:5841.
[6] Plummer CJG, Béguelin P, Kausch H-H. Colloids Surf A 1999;153:551.
[7] Wu S. J Appl Polym Sci 1988;35:549.
[8] Wu S. Polymer 1985;26:1855.
[9] Borggreve RJM, Gaymans RJ, Schuijer J, Ingen Housz JF. Polymer 1989;28:1489.
[10] Bartczack Z, Argon AS, Cohen RE, Weinberg M. Polymer 1999;40:2347.
[11] Bartczack Z, Argon AS, Cohen RE, Weinberg M. Polymer 1999;40:2331.
[12] Baker RA, Koller LL, Kummer PE. In: Katz HS, Milevski JV, editors. Particle toughening of PP in handbook of fillers for plastics. New York: Van Nostrand Rheinhold Co; 1987.
[13] Fu Q, Wang G. Polym Engng Sci 1992;32:94.
[14] Badran BM, Galeski A, Kryszewski M. J Appl Polym Sci 1982;27:3669.
[15] Patent WO 92/02681; 2002.
[16] Béguelin P, Kausch H-H. Techniques for high speed testing. In: Williams JG, Pavan A, editors. Impact and dynamic fracture of polymers and composites. London: Mechanical Engineering Publications; 1995.
[17] Béguelin P, Plummer CJG, Kausch H-H. Deformation in rubber toughened PMMA. In: Shonaike GO, Simon GP, editors. Polymer blends and alloys. New York: Marcel Dekker; 1999.
[18] Williams JG. Fracture mechanics of polymers. Chichister, UK: Ellis Horwood; 1984.
[19] Williams JG. European Structural Integrity Society Test protocol TC4; 1990.
[20] Irwin GR. J Appl Mech 1957;24:361.
[21] Wunderlich B, Macromolecular physics, vol. 1. New York: Academic Press; 1973.
[22] Holmes DR, Bunn CW, Smith DJ. J Polym Sci 1955;17:159.
[23] Murthy NS, Bray RG, Correale ST, Moore RA. Polymer 1995;36:3863.
[24] Rotter G, Ishida H. J Polym Sci, Polym Phys 1992;30:489.
[25] Penel-Pierron L, Depecker C, Séguéla R, Lefebvre J-M. J Polym Sci, Polym Phys 2000;39:484.
[26] Hoashi K, Andrews RD. J Polym Sci, Polym Symp 1972;38:387.
[27] Papir YS, Kapur S, Rogers CE, Bauer E. J Polym Sci, Polym Phys 1972;10:1305.